Geophysical Journal International

Geophys. J. Int. (2011) **184,** 1167–1179 doi: 10.1111/j.1365-246X.2010.04893.x

Hydraulic conductivity in spatially varying media—a pore-scale investigation

J. Jang,[1] G. A. Narsilio[2] and J. C. Santamarina[3]

[1] *School of Civil and Environmental Engineering, 790 Atlantic Drive, Georgia Institute of Technology, Atlanta, GA 30332, USA. E-mail: jjang6@gatech.edu*
[2] *Department of Infrastructure Engineering, The University of Melbourne, Parkville, VIC 3010, Australia*
[3] *School of Civil and Environmental Engineering, 790 Atlantic Drive, Georgia Institute of Technology, Atlanta, GA 30332, USA*

Accepted 2010 November 14. Received 2010 August 28; in original form 2009 November 13

GJI Marine geosciences and applied geophysics

SUMMARY

The hydraulic conductivity can control geotechnical design, resource recovery and waste disposal. We investigate the effect of pore-scale spatial variability on flow patterns and hydraulic conductivity using network models realized with various tube size distributions, coordination number, coefficient of variation, correlation and anisotropy. In addition, we analyse flow patterns to understand observed trends in hydraulic conductivity. In most cases, the hydraulic conductivity decreases as the variance in pore size increases because flow becomes gradually localized along fewer flow paths; as few as 10 per cent of pores may be responsible for 50 per cent of the total flow in media with high pore-size variability. Spatial correlation reduces the probability of small tubes being next to large ones and leads to higher hydraulic conductivity while focused fluid flow takes place along interconnected regions of high conductivity. A pronounced decrease in tortuosity is observed when pore size and spatial correlation in the flow direction are higher than in the transverse direction. These results highlight the relevance of grain size and formation history dependent pore size distribution and spatial variability on hydraulic conductivity, related geo-process and engineering applications.

Key words: Numerical solutions; Hydrology; Microstructure; Permeability and porosity.

1 INTRODUCTION

The hydraulic conductivity k depends on the size of pores, their spatial distribution and connectivity. These pore-scale characteristics are defined by grain size distribution and formation history. In turn, hydraulic conductivity controls fluid invasion, flow rate and pore fluid pressure distribution. Consequently, hydraulic conductivity affects storativity, effective stress and mechanical stability, plays a critical role in geotechnical design, determines contaminant migration and the selection of remediation strategies, defines the limits for resource recovery (oil production and residual oil saturation, gas extraction from hydrate bearing sediments, methane recovery from coal bed methane, non-isothermal fluid flow in geothermal applications), and is a central parameter in the design of waste disposal strategies, from nuclear waste to CO_2 sequestration.

In this study, we investigate the effect of pore-scale spatial variability on macroscale hydraulic conductivity using network models, following the pioneering work by Fatt (1956a,b,c). The main advantage of network models resides in their ability to capture pore-scale characteristics within a physically sound upscaling algorithm to render macroscale properties relevant to the porous medium. Networks can be generated either by assuming an idealized regular geometry, by adopting physically representative networks that capture the porous structure (Bryant *et al.* 1993) or by mapping the pore structures measured by high resolution tomographic technics onto a network structure (Dong & Blunt 2009, see also Al-Raoush & Wilson 2005; Narsilio *et al.* 2009). Network model results are consistent with experimentally obtained values of permeability (Al-Kharusi & Blunt 2007; Al-Kharusi & Blunt 2008). The approach has been used to upscale a wide range of pore-scale phenomena such as viscous drag, capillarity, phase change (e.g. ice or hydrate) and mineral dissolution. Consequently, network models have been used to study multiphase flow (Valvatne 2004; Al-Kharusi & Blunt 2008), wettability effects in multiphase flow (Suicmez *et al.* 2008), fine migration and clogging (Kampel *et al.* 2008), mineral dissolution (Hoefner & Fogler 1988; Fredd & Fogler 1998), pressure-induced pore closure (David 1993), CO_2 sequestration (Kang *et al.* 2005), liquid or gas diffusion through porous media (Laudone *et al.* 2008; Mu *et al.* 2008), drying and unsaturation (Prat 2002; Surasani *et al.* 2008), the effect of flow localization on diffusion (Bruderer & Bernabé 2001) and resource recovery such as methane production from hydrate bearing sediments (Tsimpanogiannis & Lichtner 2003; Tsimpanogiannis & Lichtner 2006). Furthermore, pore-scale network models have been coupled to continuum models to conduct field-scale simulations of complex processes such as clogging, reactive flow and non-Darcian flow near well-bores (Balhoff *et al.* 2007).

The first part of the manuscript summarizes previous studies. Then, we provide a detailed description of the numerical model, report statistical results in terms of equivalent hydraulic conductivity and compare trends against known and analytically derived lower and upper bounds.

2 VARIABILITY IN HYDRAULIC CONDUCTIVITY—PREVIOUS STUDIES

Hydraulic conductivity can vary by more than 10 orders of magnitude, from very low values in montmorillonitic shale to high values in gravels and boulders. Hydraulic conductivity varies widely even for a given material. The coefficient of variation, defined as the ratio between the standard deviation and the mean, can range from 100 to 800 per cent for both natural sediments (Libardi *et al.* 1980; Warrick & Nielsen 1980; Cassel 1983; Albrecht *et al.* 1985; Duffera *et al.* 2007) and remolded sediments (Benson 1993; Benson & Daniel 1994). Data are typically log-normal distributed so that $x = \log(k/[k])$ is Gaussian, where $[k]$ captures the dimensions of k (Freeze 1975; Hoeksema & Kitanidis 1985).

The correlation length L is the distance where the spatial autocorrelation decays by $1/e \cong 0.368$. The correlation length for hydraulic conductivity ranges from less than a meter to hundreds of meters. It is typically longer in the horizontal plane than in the vertical direction, in agreement with layering and weathering patterns (Ditmars *et al.* 1988; Bjerg *et al.* 1992; DeGroot 1996; Lacasse & Nadim 1996).

The equivalent hydraulic conductivity k_{eq} of spatially varying media reflects the distribution of individual values k_i, their spatial correlation and flow conditions. Available close-form solutions are summarized in Table 1. In particular, the equivalent hydraulic conductivity k_{eq} is (1) the harmonic mean of individual k_i values in 1-D systems, (2) the geometric mean in 2-D media and (3) higher than the geometric mean when seepage in 3-D systems can take place

Table 1. Equivalent hydraulic conductivity-mixture models and bounds.

Equivalent, k_{eq}		Assumptions/comments	References
$k_a = \sum_{i=1}^{N} t_i k_i \Big/ \sum_{i=1}^{N} t_i$	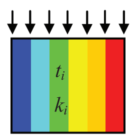	Arithmetic mean—parallel Parallel stratified media Upper bound	Wiener (1912)
$k_h = \sum_{i=1}^{N} t_i \Big/ \sum_{i=1}^{N} \frac{t_i}{k_i}$	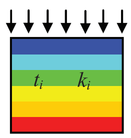	Harmonic mean—Series Perpendicular stratified media (1-D flow) Lower bound	
$k_g = \left(\prod_{1}^{N} k_i\right)^{1/N}$	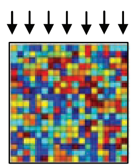	Geometric mean Lognormal k_i distribution/isotropic media (2-D flow)	Warren & Price (1961)
$k_{eq} = k_a^{\alpha} k_h^{1-\alpha} \left(\alpha = \frac{D-1}{D}\right)$		Statistically homogeneous and isotropic. Weighted average of Wiener bounds	Landau & Lifshitz (1960)
$k_a - \frac{f_1 f_0 (k_1 - k_0)^2}{k_0(D - f_0) + k_1 f_0} \le k_{eq} \le k_a - \frac{f_1 f_0 (k_1 - k_0)^2}{k_1 (D - f_1)^2 + k_0 f_1}$		Based on a model constructed of composite spheres. Isotropic binary medium. Uniform flow	Hashin & Shtrikman (1962)
if $f_0 \ge 0.5 \Rightarrow k_{eq} \ge k_{ac}$ if $f_0 \le 0.5 \Rightarrow k_{eq} \le k_{ac}$ if $f_0 = 0.5 \Rightarrow k_{eq} = \sqrt{k_1 k_0}$, where $k_{ac} = \frac{1}{2}\left[(f_1 - f_0)(k_1 - k_0) + \sqrt{(f_1 - f_0)^2 (k_1 - k_0)^2 + 4 k_1 k_0}\right]$ if $f_0 \ge 0.5 \Rightarrow k_{eq} \le k_m$ $k_m = \frac{f_1 k_0 k_1 + f_0 k_a \sqrt{k_0(2k_a - k_0)}}{f_1 m^* + f_0 \sqrt{k_0(2k_a - k_0)}}$ if $f_0 \le 0.5 \Rightarrow k_{eq} \ge k_m$ $k_m = k_0 k_1 \frac{f_0 k_a + f_1 \sqrt{k_0(2m^* - k_0)}}{f_1 k_0 k_1 + f_1 m^* \sqrt{k_0(2m^* - k_0)}}$		Isotropic 2-D random two phase mosaic medium. Uniform flow.	Matheron (1967)

Note: k_{eq} is the equivalent hydraulic conductivity; f_0 and f_1 are the fractions of the medium with hydraulic conductivity k_0 and k_1, where $k_1 > k_0$, D is the space dimension (i.e. 1, 2 or 3); $m^* = f_1 k_0 + f_0 k_1$.

through multiple alternative flow paths. The equivalent hydraulic conductivity in these three cases can be computed in terms of the geometric mean k_g and the variance σ^2 in $\log(k/[k])$, as captured in the following expressions (Gutjahr *et al.* 1978; Dagan 1979—refer to Table 1):

$$k_{eq} = k_h = k_g \left[1 - \left(\sigma^2_{\log k}/2\right)\right] \quad \text{(1-D system)} \tag{1}$$

$$k_{eq} = k_g \quad \text{(2-D system)} \tag{2}$$

$$k_{eq} = k_g \left[1 + \left(\sigma^2_{\log k}/6\right)\right] \quad \text{(3-D system).} \tag{3}$$

More complex systems have been studied using equivalent continuum numerical methods. Those results show that (1) flow rate decreases as the coefficient of variation COV(k) increases and (2) the mean hydraulic conductivity in correlated fields is higher than in uncorrelated fields with the same coefficient of variation COV(k) (Griffiths & Fenton 1993; Griffiths *et al.* 1994; Griffiths & Fenton 1997).

3 NETWORK MODELS

Network models consist of tubes connected at nodes and can be used to simulate fluid flow through pervious materials. Volume can be added at nodes to reproduce various conditions (Reeves & Celia 1996; Blunt 2001; Acharya *et al.* 2004). The flow rate through a tube q [m^3 s^{-1}] is a function of fluid viscosity η [Ns m^{-2}], tube radius R [m], tube length ΔL [m] and pressure difference between end nodes ΔP [N m^{-2}]

$$q = \frac{\pi R^4}{8\,\eta\,\Delta L}\Delta P = \alpha\,\Delta P \quad \text{tube equation} - \text{Poiseuille,} \tag{4}$$

where $\alpha = \pi R^4/(8\eta\Delta L)$ under isothermal condition, constant viscosity and constant tube radius. Mass conservation requires that the total flow rate into a node equals the total flow rate out of the node

$$\sum q_i = 0 \quad \text{node equation.} \tag{5}$$

Eqs (4) and (5) can be combined to determine the pressure at a central node P_c as a function of the pressure at neighbouring nodes P_i.

$$P_c = \frac{\sum \alpha_i P_i}{\sum \alpha_i}. \tag{6}$$

If all α-values are equal, eq. (6) predicts $P_c = (P_a + P_b + P_r + P_l)/4$. It is worth noting that this equation is identical to the first-order central finite difference formulation of Laplace's field equation.

Eq. (6) is written at all internal nodes to obtain a system of linear equations which can be captured in matrix form

$$AP = B, \tag{7}$$

where the matrix A is computed with tube conductivities α, P is the vector of unknown pressures at internal nodes and the vector B captures known boundary pressures. The vector P can be recovered as $P = A^{-1}B$. Once fluid pressures P_i are known at all nodes, the global flow rate Q through the network is obtained by adding the flow rate q (eq. 4) in all tubes that cross a plane normal to the flow direction. The equivalent network hydraulic conductivity in the direction of the prescribed external pressure gradient is calculated from the computed flow rate Q and the imposed pressure gradient between inlet and outlet boundaries. Insightful information is gained by analysing prevailing flow patterns within the networks as will be shown later in this manuscript.

Networks are realized with pre-specified statistical characteristics. We control the coefficient of variation in tube size, spatial correlation and isotropy to generate networks with different tube size distribution (monosized, bimodal or log-normal distributed) spatially uncorrelated or correlated and isotropic or anisotropic. Every realization is identified according to these three qualifiers.

Pore size R is log-normally distributed in sediments. Mercury intrusion porosimetry data for a wide range of soils and effective stress conditions show that the standard deviation in $\sigma[\ln(R/[\mu\text{m}])]$ is about 0.4 ± 0.2. Examples of statistical distributions used in this study are shown in Fig. 1. Throughout the manuscript, the log-normal distribution of pore cross sectional area is used in terms of R^2, that is, $\log(R^2/[\text{R}]^2)$ where [R] indicates unit of R. Tube R^2 values are generated as $R^2 = 10^a$ where a is a set of Gaussian distributed random numbers with given standard deviation. Values R^2 are scaled to satisfy the selected mean value. While we assume

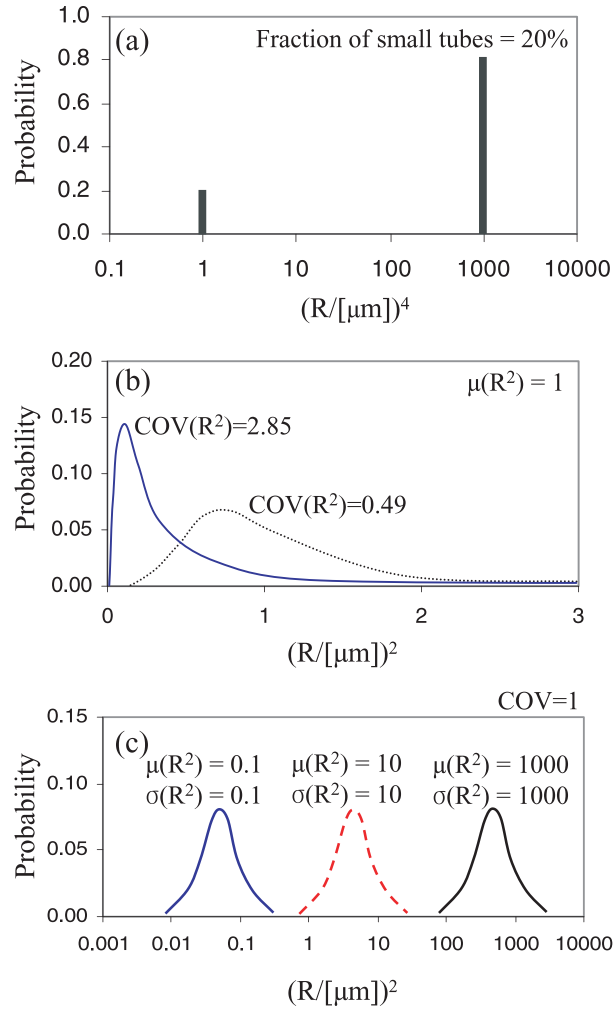

Figure 1. Schematic of typical distribution of R^2 in spatially varying fields. (a) Bimodal distribution of tubes (used in Figs 2 and 3) when fraction of small tubes is 20 per cent. The relative size of large to small tube radii is $(R_L/R_S)^4 = 10^3$. (b) Two distributions of tube size R^2 with the same $\mu(R^2)$ but different standard deviation used in Figs 4, 6 and 7. As the coefficient of variation increases, the distribution of R^2 is skewed to the right. (c) Distributions of R^2 used in Fig. 5. Note that $\sigma(R^2)$ of two sets of tube size distribution with different $\mu(R^2)$ are adjusted to have same COV(R^2).

log-normal distribution for network generation, we analyse results and global trends in terms of the mean and standard deviation of R^2, that is $\mu(R^2)$ and $\sigma(R^2)$ for each realization.

The computer code is written in MATLAB. The run time for each realization in a 2.4 GHz processor is ∼40 min. The reported study was conducted using a stack of dual-core computers.

4 STUDIED CASES—NUMERICAL RESULTS

Network models are used herein to extend previous studies on the effect of spatial variability and anisotropy on hydraulic conductivity. Numerical results are presented next. Simulation details are listed in the corresponding figure captions.

4.1 Bimodal distribution—effect of coordination number and bounds

Consider a bimodal distribution made of large and small tubes of relative size $R_L/R_S = 5.62$ so that their conductivity ratio is $k_L/k_S = 10^3$ for constant tube length (refer to eq. 4). 20 spatially randomly arranged networks are generated for each fixed fraction of small tubes. 2-D networks with coordination number, $cn = 4$, 6 and 8 and 3-D networks with coordination number $cn = 6$ are used to

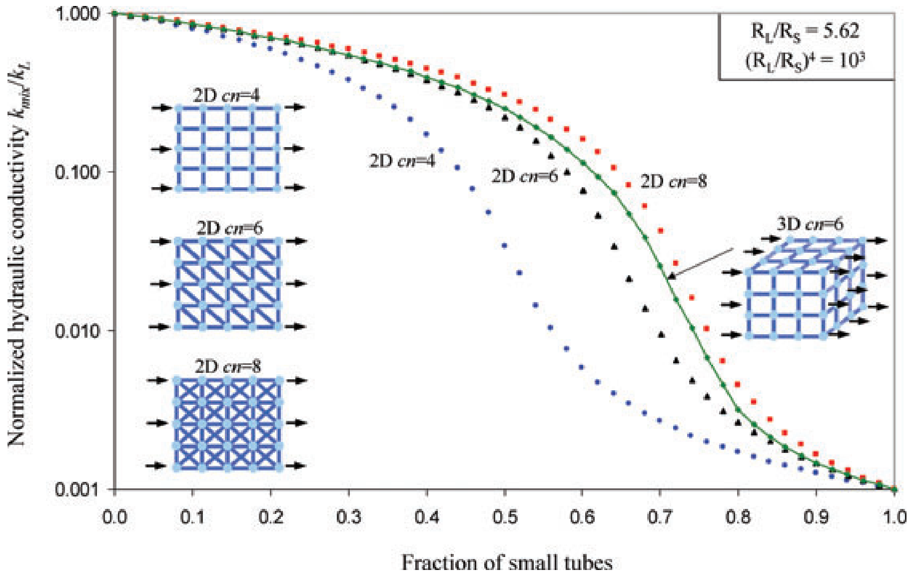

Figure 2. Effect of coordination number cn on equivalent hydraulic conductivity in bimodal distribution k_{mix} normalized by the hydraulic conductivity in the field composed of only large tubes k_L. Each point is the average value of 20 realizations. Bimodal distribution of tubes. The relative size of large L to small S tube radii is $(R_L/R_S)^4 = 10^3$. 2-D network model: 50 × 50 nodes, 4900 tubes and $cn = 4$ (circle)/$cn = 6$ (triangle)/$cn = 8$ (square). 3-D network model: 15 × 15 × 15 nodes, 9450 tubes and $cn = 6$ (diamond).

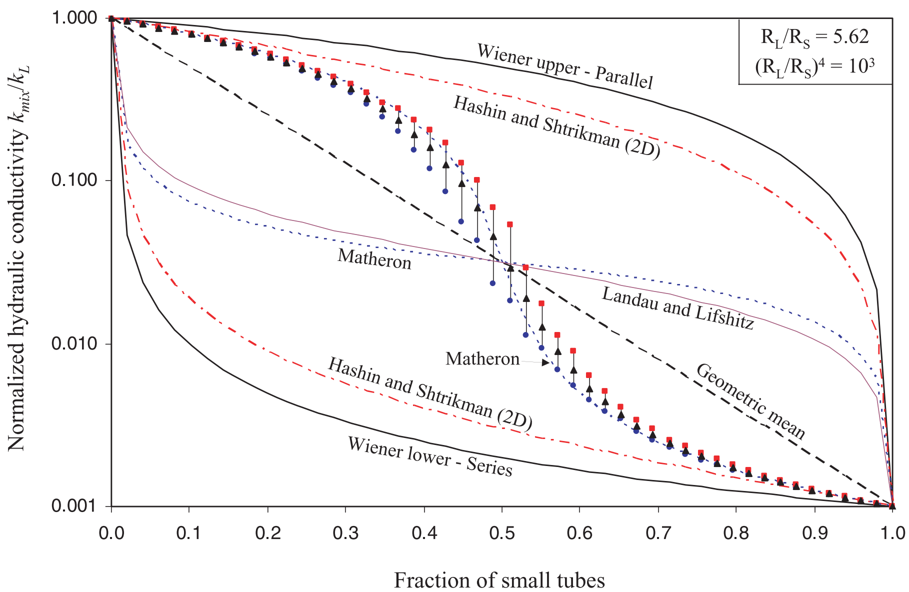

Figure 3. Computed equivalent hydraulic conductivity in bimodal distribution k_{mix} normalized by the hydraulic conductivity in the field composed of only large tubes k_L, models and bounds as a function of the fraction of small tubes. Points represent the maximum (square), average (triangle) and minimum (circle) values of 20 realizations at each fraction of small tubes. Bounds and models are described in Table 1. 2-D network model: 50 × 50 nodes, 4900 tubes, bimodal distribution of tubes, relative size of large L to small S tube radii $(R_L/R_S)^4 = 10^3$ and coordination number $cn = 4$.

investigate the effect of coordination number on flow conditions. Computed hydraulic conductivities are averaged for the 20 realizations and plotted in Fig. 2 where the mean value is normalized by the hydraulic conductivity of the network model made of large tubes only, k_{mix}/k_L.

Results in Fig. 2 show that network conductivity range in three orders of magnitude from $k_{mix}/k_L = 0.001$ to 1.0 in agreement with the size ratio $(R_L/R_S)^4 = 10^3$. Hydraulic conductivity values increase as the coordination number increases. There is a pronounced decrease in flow rate where large tubes cease to form a percolating path. Percolation thresholds (readily identified in linear–linear plots—see also Hoshen & Kopelman 1976) decrease as coordination numbers increase; results are consistent with reported percolation thresholds for various networks: 2-D-honeycomb (fraction of small

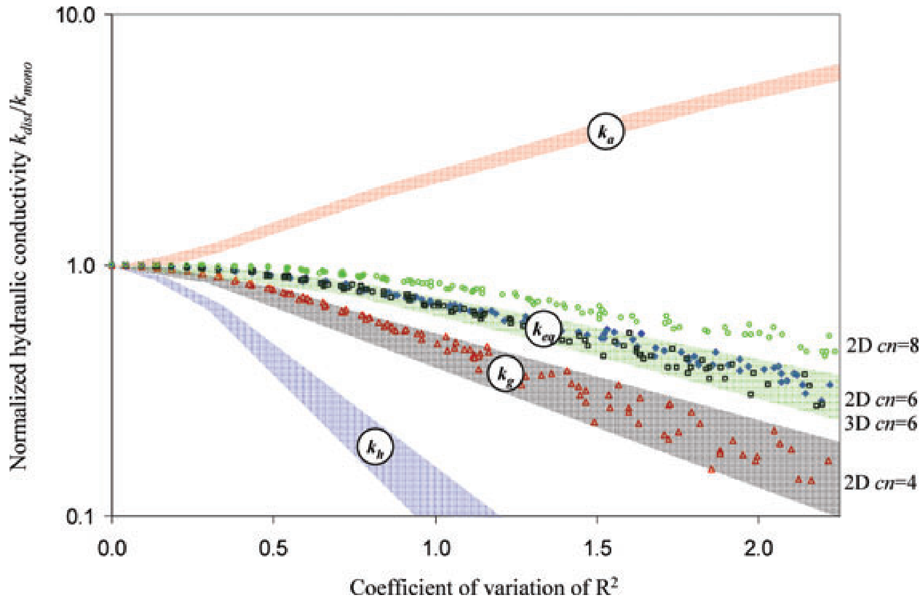

Figure 4. Equivalent hydraulic conductivity in uncorrelated tube network k_{dist} normalized by the hydraulic conductivity for the monosized tube network k_{mono} as a function of the coefficient of variation of R^2. Each point is a single realization. All realizations have the same $\mu(R^2)$. 2-D network model: 50 × 50 nodes, 4900 tubes and $cn = 4$ (empty triangle), $cn = 6$ (empty square), $cn = 8$ (empty circle). 3-D network model: 15 × 15 × 15 nodes, 9450 tubes and $cn = 6$ (solid diamond). Shaded areas show arithmetic k_a, geometric k_g, harmonic k_h mean of 2-D and 3-D system and analytical solution k_{eq} of 3-D system (eq. 3).

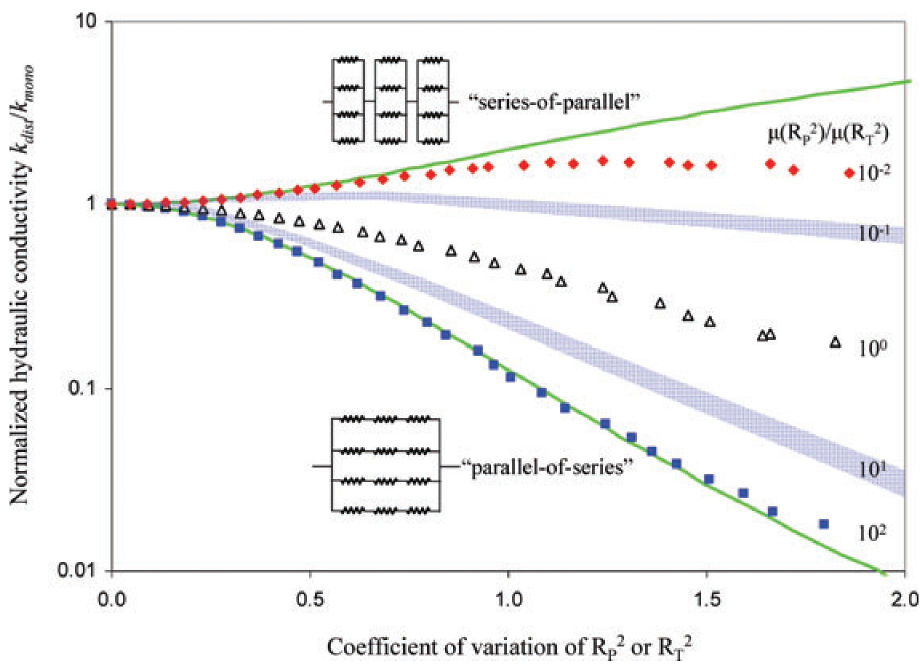

Figure 5. Anisotropic conductivity: equivalent hydraulic conductivity in uncorrelated and distributed tube network k_{dist} normalized by the hydraulic conductivity for the monosized tube network k_{mono} as a function of coefficient of variation of R^2. Normalized hydraulic conductivities are obtained at different values of the ratio between the mean tube size parallel and transverse to the flow direction $(R_P/R_T)^2$. Each point is the average value of 20 realizations (using same set of tube sizes, but different spatial distribution). For clarity, results for intermediate sequences are shown as shaded area. Normalized hydraulic conductivities in series of parallel and parallel of series circuits are also obtained. 2-D network model: 50 × 50 nodes, 4900 tubes, $cn = 4$ and log-normal distribution of R^2.

tubes = 0.65), 2-D-square (0.5), 2-D-triangular (0.35) and 3-D-simple cubic arrangement (0.25) (Stauffer & Aharony 1992; Sahimi 1994).

Analytical solutions for equivalent hydraulic conductivity and lower and upper bounds summarized in Table 1 are compared to numerical results in Fig. 3. The normalized mean hydraulic conductivity for 20 realizations using 2-D networks with $cn = 4$ follows the Matheron's mixture model. All simulation results are between Wiener's and Hashin and Shtrikman's upper and lower bounds (Table 1). Hashin and Shtrikman bounds incorporate the dimensionality of the system resulting in 3-D bounds that are shifted towards high k_{eq} values compared to 2-D bounds. Overall, numerical and analytical results point to higher value of hydraulic conductivity with a larger number of alternative flow paths.

4.2 Coefficient of variation in random networks

We explore next the effect of variance in R^2 by creating 2-D and 3-D networks with the same nominal mean $\mu(R^2)$. Network statistics, mean $\mu(R^2)$, standard deviation $\sigma(R^2)$ and coefficient of variation COV(R^2) are evaluated for each realization. Note that R^2 distributions are skewed towards higher values as the coefficient of variation increases (Fig. 1b) even though they all have the same $\mu(R^2)$.

The conductivity of a given realization k_{dist} is normalized by the conductivity k_{mono} of the network made of all equal size tubes, that is, $R^2 = \mu(R^2)$ and COV(R^2) = 0. The normalized hydraulic conductivity $k_{\mathrm{dist}}/k_{\mathrm{mono}}$ decreases as the coefficient of variation of R^2 increases (Fig. 4) (see similar results in Bernabé & Bruderer 1998). The normalized arithmetic, geometric and harmonic means computed for each network are shown as shaded areas on Fig. 4. The range in normalized hydraulic conductivities for 2-D cn = 4 networks coincides with the shaded band of geometric means computed for all networks. Computed hydraulic conductivity values for 3-D $cn = 6$ and 2-D $cn = 6$ networks are the same as the range obtained using eq. (3) and confirm the applicability of the close-form solutions.

These trends result from the increased probability of large tubes becoming surrounded by smaller tubes, that is, there is an increased probability of finding a small tube along every potential flow path with increasing coefficient of variation COV(R^2). This effect is more pronounced when the coordination number decreases because there are fewer alternative flow paths; in other words, network models with high coordination number are less sensitive to variation in pore size COV(R^2) because a higher number of alternative flow paths develop in high connectivity condition. Flow patterns are analysed in detail later in this manuscript.

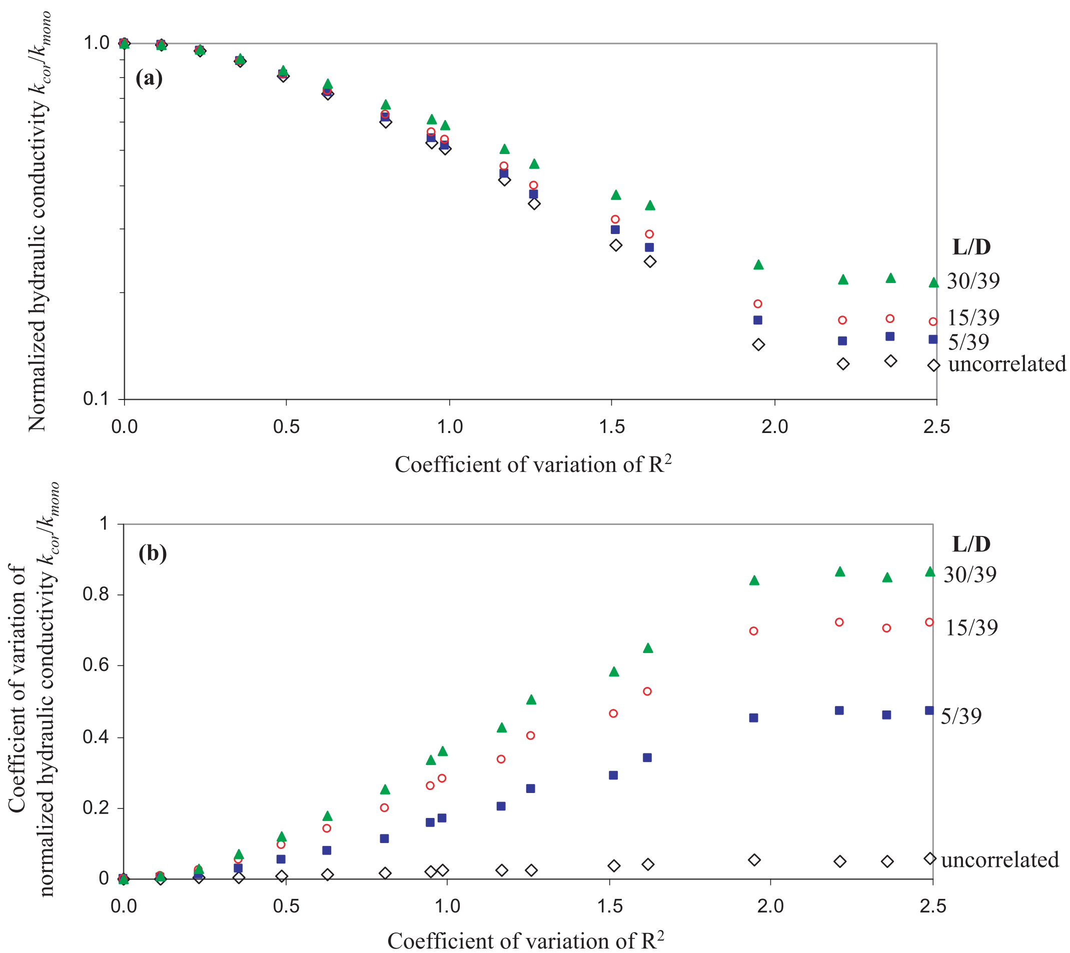

Figure 6. Correlated field. (a) Equivalent hydraulic conductivity in isotropic uncorrelated and correlated tube network k_{cor} normalized by the hydraulic conductivity for the monosized tube network k_{mono} as a function of the coefficient of variation of R^2. (b) Coefficient of variation of the equivalent hydraulic conductivities as a function of the coefficient of variation of R^2. The correlation length L is reported relative to the specimen size. Each point stands for the average of 100 realizations. 2-D network model: 40 × 40 nodes, 3120 tubes, $cn = 4$ and log-normal distribution of R^2.

4.3 Anisotropic, uncorrelated networks

When tubes parallel to the predominant fluid flow direction are monosized R_P ('parallel tubes'), the flow rate is proportional to R_P^4 and the distribution of tube size transverse to flow direction R_T ('transverse tubes') does not affect the global flow rate because there is no local gradient or fluid flow transverse to the main flow direction. This is not the case when tubes parallel to the flow direction are of different size, that is, not monosized.

Let's consider log-normal distributions for the size R_P^2 and R_T^2 of both parallel and transverse tubes. We select different mean values $\mu(R_P^2) \neq \mu(R_T^2)$ and adjust standard deviations $\sigma(R_P^2)$ and $\sigma(R_T^2)$ so that both parallel and transverse tubes have the same coefficient of variation COV(R^2).

Results in Fig. 5 show that the normalized hydraulic conductivity decreases as the coefficient of variation COV(R^2) increases when $\mu(R_P^2)/\mu(R_T^2) > 1$. However, the hydraulic conductivity may actually increase when transverse tubes are of high conductivity as shown by the $\mu(R_P^2)/\mu(R_T^2) = 10^{-2}$ case: fluid flows along transverse tubes until it finds parallel tubes of high conductivity, mostly with $R_P^2 > \mu(R_P^2)$.

Two extreme networks of 'series-of-parallel' and 'parallel-of-series' tubes provide upper and lower bounds to the numerical results (shown as lines in Fig. 5). When the ratio of $(R_P/R_T)^2$ is larger than 10^{-1}, the network responds as a parallel combination of tubes in series. When the ratio of $(R_P/R_T)^2$ is smaller than 10^{-1}, pressure is homogenized along the relatively large transverse tubes, as captured in the series-of-parallel bound.

4.4 Spatial correlation in pore size—isotropic networks

Spatial correlation in pore size upscales to the macroscale hydraulic conductivity in unexpected ways. The methodology followed in this study starts with a set of tubes with fixed $\mu(R^2)$ and COV(R^2). Then, we use the same set of tubes to generate 100 randomly redistributed spatially uncorrelated networks and other three sets of 100 isotropically correlated networks with correlation lengths $L/D = 5/39$, $15/39$

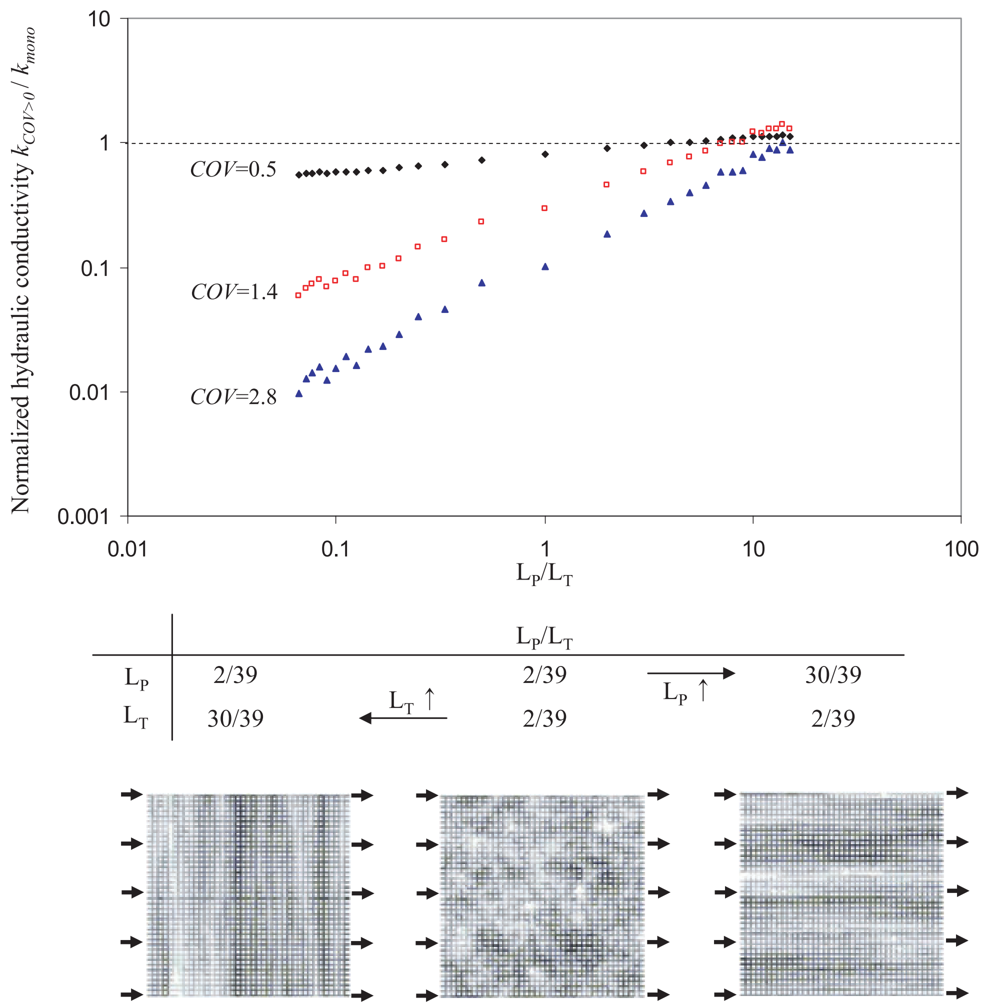

Figure 7. Effect of anisotropic correlation on equivalent hydraulic conductivity in an anisotropically correlated tube network $k_{\mathrm{COV}>0}$ normalized by the hydraulic conductivity for the monosized tube network $k$mono. Three sets of tubes different COV(R^2) are generated and used to form correlated fields of different anisotropic correlation length. L_P and L_T are the correlation lengths parallel and transverse to flow direction. D is the length of medium perpendicular to the flow direction. In the range between $L_P/L_T = 0.01$–1, $L_P = 2D/39$ fixed and L_T changes from $2D/39$ to $30D/39$. In the range between $L_P/L_T = 1$–100, $L_T = 2D/39$ fixed and L_P changes from $2D/39$ to $30D/39$. Each point is an average of 20 realizations. 2-D network model: 40×40 nodes, 3120 tubes, $cn = 4$ and log-normal distribution of R^2.

and 30/39 (where L is correlation length and D is the network size transverse to the overall flow direction) and for different COV(R^2). We use the method by Taskinen *et al.* (2008) to create correlated fields.

Hydraulic conductivities are numerically computed for all networks k_{cor}. For comparison, the hydraulic conductivity k_{mono} is evaluated for a network of equal size tubes, that is, COV(R^2) = 0. The normalized mean hydraulic conductivity $k_{\mathrm{cor}}/k_{\mathrm{mono}}$ computed using the 100 realizations for each COV(R^2) is plotted versus COV(R^2) in Fig. 6a. The normalized mean conductivity decreases with COV(R^2) in all cases in agreement with Fig. 4, but it is higher in correlated than in uncorrelated networks. Note that the variance from the mean trend also increases with COV(R^2) and it is exacerbated by spatial correlation L/D (Fig. 6b).

4.5 Spatial correlation in pore size—anisotropic networks

To gain further insight into the previous results, we study the effect of anisotropy in correlation length following a similar approach, but in this case we distinguish the correlation length parallel to the overall flow direction L_{P} from the correlation length transverse to the overall flow direction L_{T}. The isotropic case is created with $L_{\mathrm{P}}/D = L_{\mathrm{T}}/D = 2/39$ so that $L_{\mathrm{P}}/L_{\mathrm{T}} = 1.0$. High correlation parallel to the flow direction is simulated by increasing L_{P}/D, while high correlation transverse to the flow direction is imposed by increasing L_{T}/D. The study is repeated for three sets of R^2 with COV(R^2) = 0.5, 1.4 and 2.8.

Average hydraulic conductivity values (based on 20 realizations) are normalized by the hydraulic conductivity k_{mono} of the network made of equal size tubes. Results in Fig. 7 show that the normalized hydraulic conductivity $k_{\mathrm{COV}>0}/k_{\mathrm{mono}}$ increases as spatial correlation parallel to the flow direction $L_{\mathrm{P}}/L_{\mathrm{T}}$ increases and it may even exceed the conductivity of the monosized tube network in highly anisotropic networks with very high $L_{\mathrm{P}}/L_{\mathrm{T}}$ values. Otherwise, variation in tube size COV(R^2) has a similar effect reported previously: an increase in COV(R^2) causes a decrease in hydraulic conductivity (see Figs 4 and 6). Overall, results in Fig. 7 point to pore-scale flow conditions similar to those identified in Fig. 5.

5 DISCUSSION

Numerical results show the evolution of percolation in bimodal system (Figs 2 and 3) and the decrease in hydraulic conductivity with increasing variance in pore size while the mean value of pore size remains constant. This is observed for all types of network topology (Fig. 4) and in both spatially correlated and uncorrelated networks (Fig. 6). The only exception to this trend is found in highly anisotropic porous media in the direction that favours fluid flow (Figs 5 and 7).

To facilitate the visualization of flow patterns, we compute tube flow rates (eq. 4) and represent tubes with lines of thickness proportional to flow rate (additional plotting details are noted in figure captions). Fig. 8(a) shows flow patterns in bimodal distribution networks made of different fractions of small tubes. Flow localizes

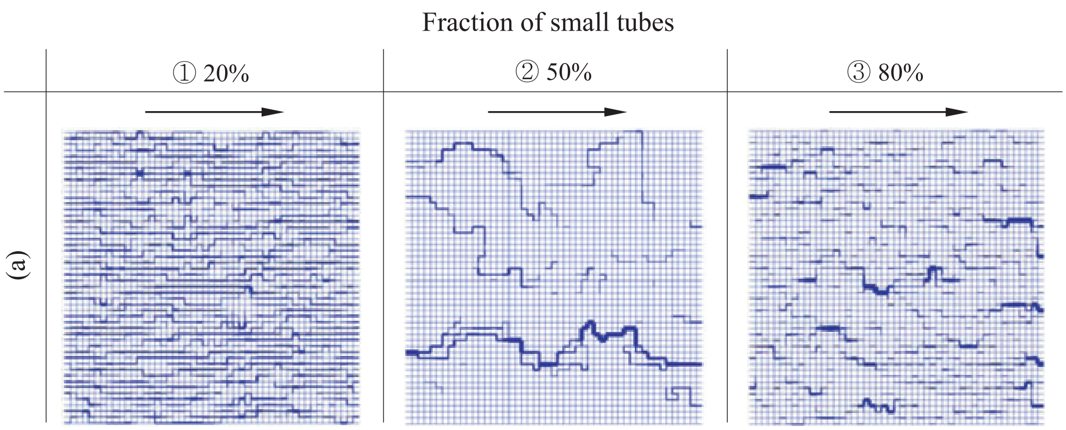

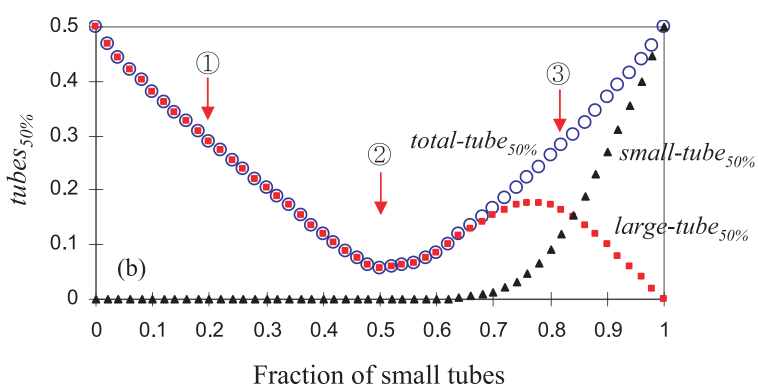

Figure 8. Analysis of flow pattern in network model of bimodal distribution of R^2 (2-D $cn = 4$ – Percolation occurs when the fraction of small tubes is 0.5. Refer to Figs 2 and 3 for simulation details). (a) Flow intensity in each tube of the network of different fraction of small tubes. The change of flow pattern in each fraction of small tubes is well detected. The arrow indicates the predominant fluid flow direction. (b) Fraction of tubes tube$_{50\ \mathrm{per\ cent}}$ responsible for 50 per cent of total conductivity. The fraction total-tube$_{50\ \mathrm{per\ cent}}$ is the summation of small-tube$_{50\ \mathrm{per\ cent}}$ and large-tube$_{50\ \mathrm{per\ cent}}$.

along dominant flow channels when the fraction of small tubes is 50 per cent, which is near the percolation threshold for this network (2-D $cn = 4$). Few flow paths are responsible for the global conductivity in networks where the fraction of either small or large tubes is ∼50 per cent (Fig. 8a②); conversely, multiple flow paths contribute to the global conductivity in networks made of a majority of either small or large tubes (Fig. 8a① and ③).

The fraction of parallel tubes, which conducts 50 per cent of the total flow, $\text{tubes}_{50\text{ per cent}}$, quantifies this observation (Fig. 8b). The values is $\text{tubes}_{50\text{ per cent}} = 50$ per cent when all tubes are of the same size, either large or small, which means flow is homogeneous. Fluid preferentially flows along the large tubes so that large tubes are responsible for 50 per cent of the total flow until the fraction of small tubes exceeds ∼65 per cent. The participation of small tubes starts to increase above the large-tube percolation threshold (0.5 – Point ② in Fig. 8b). In general, flow always seeks the larger tubes.

Distributed tube diameters exhibit a similar response. Most parallel tubes contribute to total flow when the coefficient of variation of R^2 is low (Fig. 9a①). Flow becomes gradually localized as COV(R^2) increases and fewer channels contribute to global flow ($\text{tubes}_{50\text{ per cent}}$ in Fig. 9c). Consequently, hydraulic conductivity decreases as shown earlier (Figs 4 and 6). The main effect of spatial correlation is to channel flow along interconnected regions of high conductivity (compare Figs 9a and b, see also Bruderer-Weng *et al.* 2004 for the effect of different correlation lengths on flow channelling).

Flow patterns in anisotropic networks are shown in Figs 10 and 11 for 18 realizations with different degrees of anisotropy $\mu(R_P^2)/\mu(R_T^2)$, spatial correlation L_P/L_T and tube size variability COV(R^2). The number of parallel tubes responsible for 50 per cent of the total flow is included in Fig. 12 for all cases. Significant flow takes place along transverse tubes when transverse tubes are much more conductive than parallel tubes $\mu(R_P^2) \ll \mu(R_T^2)$ (Fig. 10a), or when there is high transverse correlation $L_P/L_T \ll 1$ (Fig. 11a—upper bound was labelled ‘series-of-parallel’ configuration in Fig. 5). On the other hand, there is virtually no flow

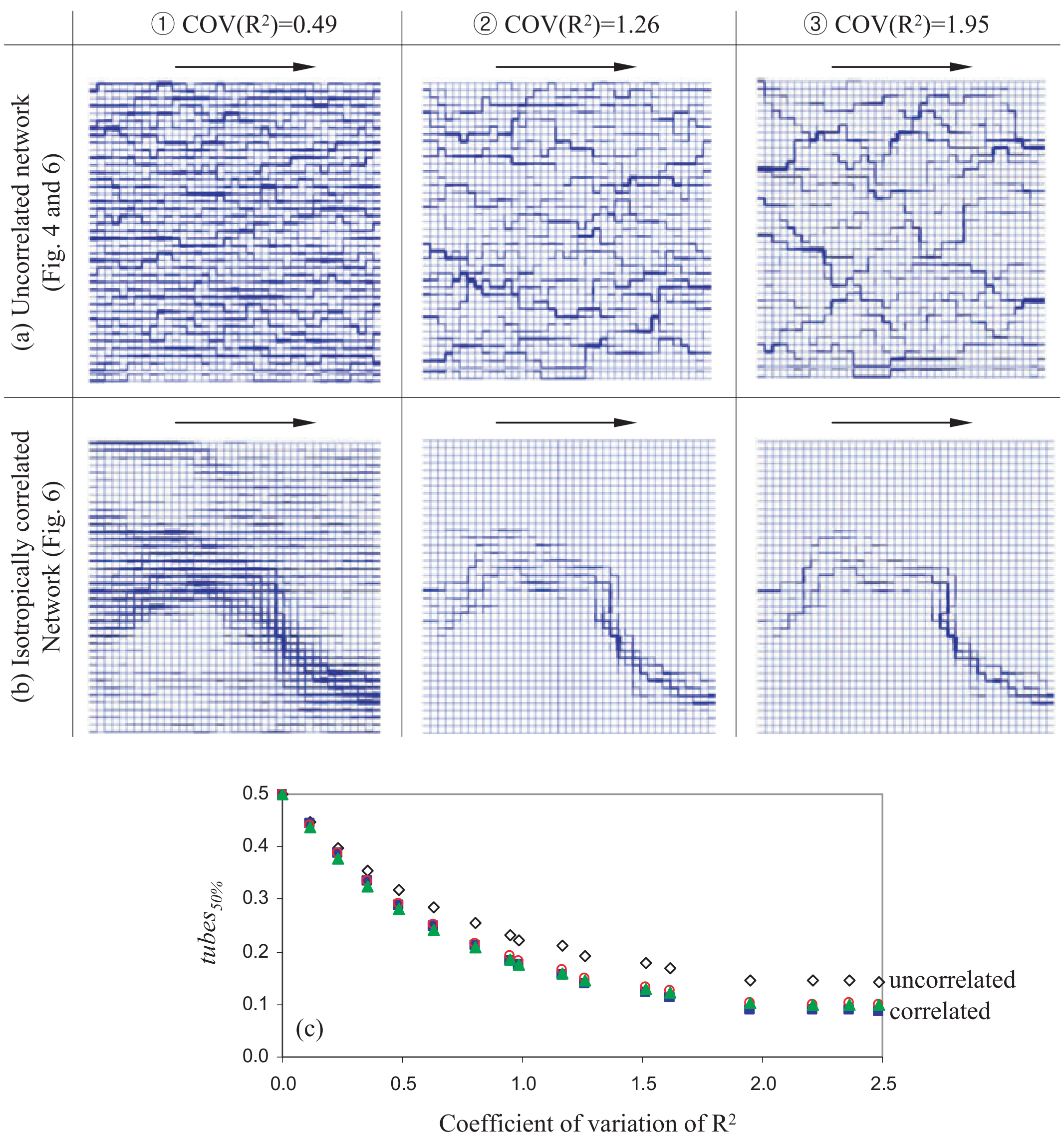

Figure 9. Analysis of flow pattern in network model of log-normal distribution of R^2 (refer to Figs 4 and 6 for simulation details). (a) Flow intensity in each tube in spatially uncorrelated network. (b) Flow intensity in each tube in spatially correlated networks. Thickness of line represents the intensity of flow rate. (c) Fraction of tubes $\text{tube}_{50\text{ per cent}}$ responsible for 50 per cent of total conductivity.

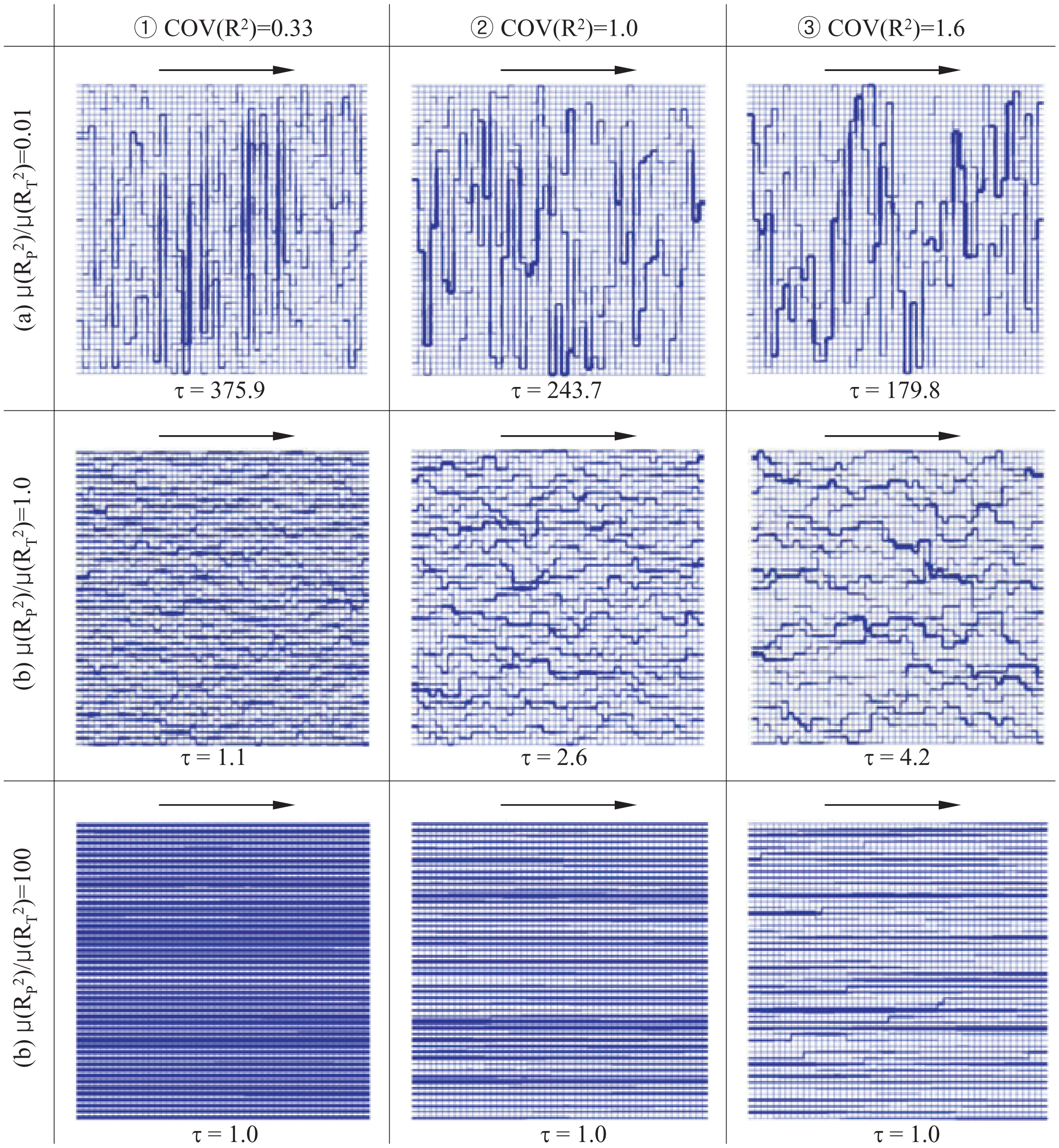

Figure 10. Analysis of flow patterns in anisotropic networks made of tubes with the same mean size $\mu(R^2)$ but different variance in size as captured in COV(R^2) (refer to Fig. 5 for simulation details). Anisotropy ratios: (a) $\mu(R_\mathrm{P}^2)/\mu(R_\mathrm{T}^2) = 0.01$, (b) $\mu(R_\mathrm{P}^2)/\mu(R_\mathrm{T}^2) = 1.0$, (c) $\mu(R_\mathrm{P}^2)/\mu(R_\mathrm{T}^2) = 100$. The arrow indicates the global flow direction. The line thickness used to represent the tubes is proportional to the flow intensity in each tube. Tortuosity values τ are shown for each case.

along transverse paths when parallel tubes are much larger than the transverse tubes $\mu(R_\mathrm{P}^2) \gg \mu(R_\mathrm{T}^2)$ (Fig. 10c) or when there is high longitudinal correlation $L_\mathrm{P}/L_\mathrm{T} \gg 1$ (Fig. 11c); in these cases, flow localizes along linear flow paths and global conductivity is limited by the smallest tubes along their longitudinal paths (third row in Figs 10 and 11—referred to the 'parallel-of-series' bound in Fig. 5). Therefore, the number of parallel tubes responsible for most of the flow decreases with increasing COV(R^2) in this case as well.

Let's define the network tortuosity factor as the ratio $\tau = (N_\mathrm{CP}/N_\mathrm{hom})^2$ between the total number of tubes in the backbone of the critical path N_CP and the number of tubes in a straight streamline parallel to the global flow direction N_hom (details in David 1993). A critical path analysis in terms of tube flow rate is used to compute the tortuosity factors for fluid flow (see Bernabé & Bruderer 1998). Figs 10 and 11 show flow patterns and associated tortuosity values. In agreement with visual patterns, there is a pronounced decrease in tortuosity when $\mu(R_\mathrm{P}^2) \gg \mu(R_\mathrm{T}^2)$ in anisotropic uncorrelated fields (Fig. 10) or when $L_\mathrm{P}/L_\mathrm{T} \gg 1$ in anisotropic correlated fields with high COV(R^2) (Fig. 11).

Spatial correlation reduces the probability of small tubes being next to large ones and leads to more focused channelling of fluid flow through the porous network. This can be observed by visual inspection of cases shown in Fig. 11 in comparison to the corresponding ones in Fig. 10.

Simple geometrical analyses show that the distance between adjacent pore centres is $2R$ for simple cubic packing and face-centred cubic packing and $\sqrt{1.5}R$ for tetrahedral packing, where R is the grain radius (see also Lindquist *et al.* 2000). However, the constant tube length assumption made in this study is only an idealization for real sediments (Bryant *et al.* 1993). For example, the distance between adjacent pore centres in Fontainebleau and Berea sandstones ranges from 20 to 600 μm with most tube lengths between 130 and 200 μm (Lindquist *et al.* 2000; Dong & Blunt 2009).

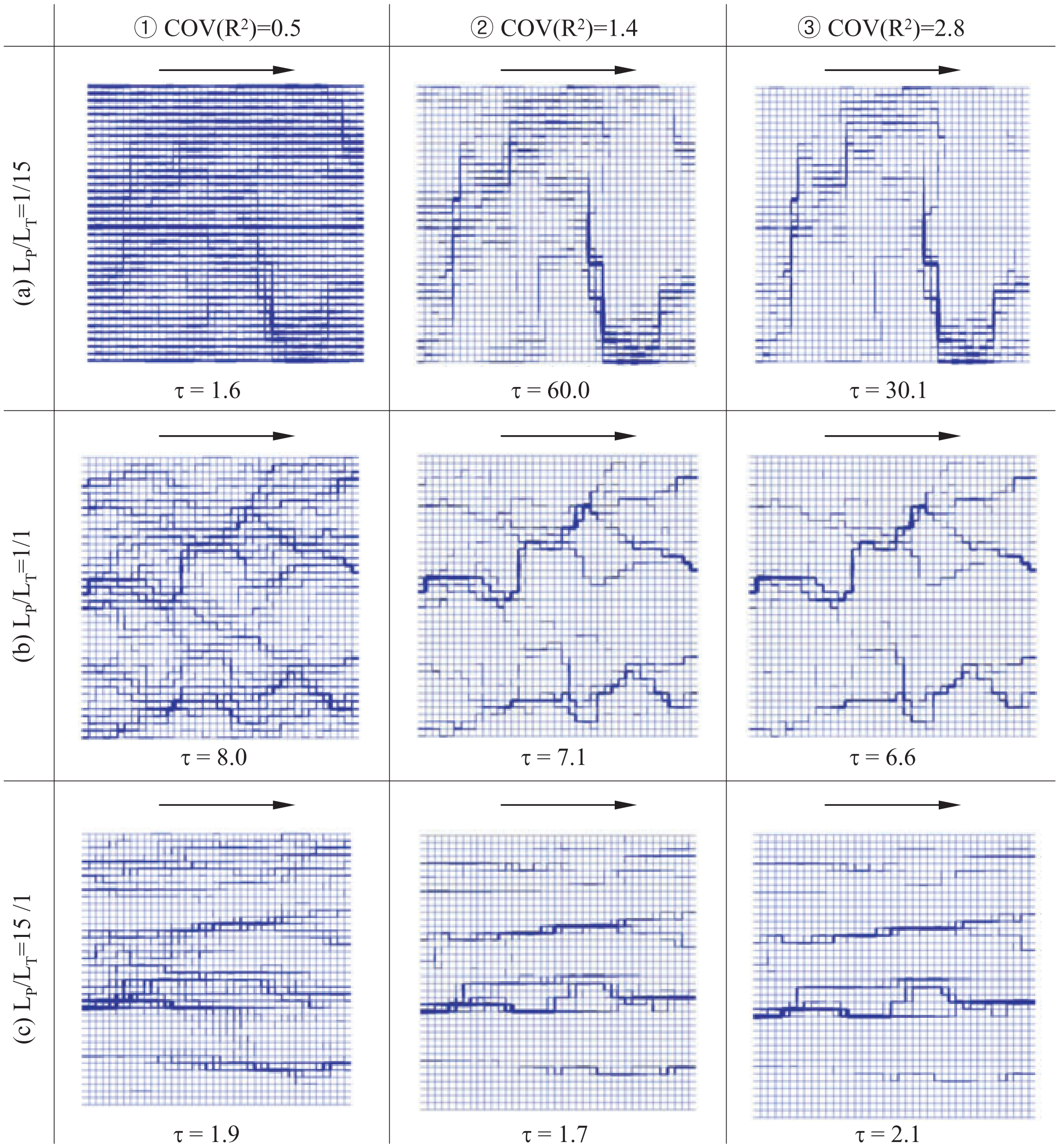

Figure 11. Analysis of flow pattern in anisotropically correlated networks made of three sets of tube areas with different COV(R^2) (refer to Fig. 7 for simulation details). Anisotropy ratios: (a) $L_P/L_T = 1/15$, (b) $L_P/L_T = 1/1$ and (c) $L_P/L_T = 15/1$. The arrow indicates the global flow direction. The line thickness used to represent the tubes is proportional to the flow intensity in each tube. Tortuosity values τ are shown for each case.

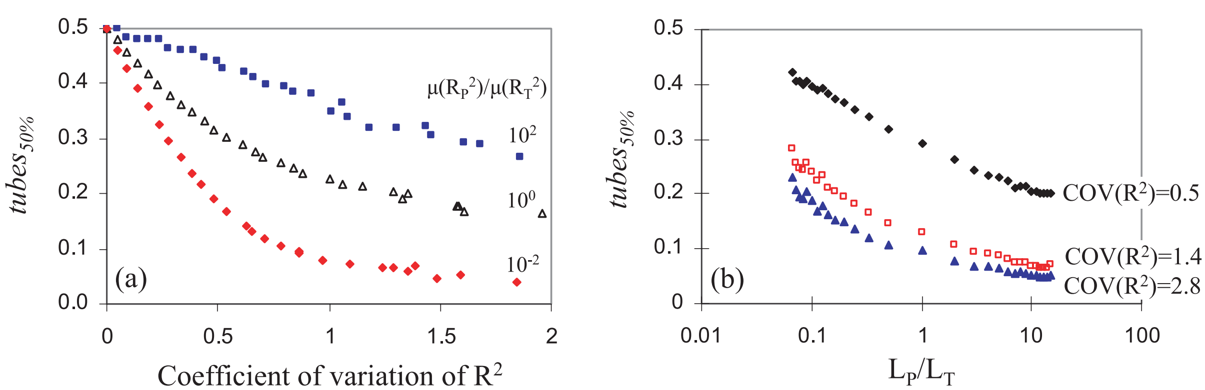

Figure 12. Fraction of tubes tubes$_{50\text{ per cent}}$ carrying 50 per cent of the total flux as a function of (a) coefficient of variation of R^2 in anisotropically uncorrelated field and (b) the ratio of parallel to transverse correlation length L_P/L_T.

While pore-to-pore distance varies in real sediments, we note that the hydraulic conductivity of tubes is much more dependent on the radius than on the tube length (see eq. 4). Therefore, the imposed variability in tube radius causes variability in tube conductivity q that could equally capture tube length variability. Clearly, variations in tube length would imply a non-regular network topology.

6 CONCLUSIONS

Grain size and formation history dependent pore size distribution and spatial variability determine the hydraulic conductivity, immiscible fluid invasion and mixed fluid flow, resource recovery, storativity and the performance of remediation strategies. Numerical simulations with porous networks permit the study of pore-size distribution, spatial correlation and anisotropy on hydraulic conductivity and flow patterns in pervious media.

In most cases, the hydraulic conductivity decreases as the variance in pore size increases because flow becomes gradually localized along fewer flow paths. As few as 10 per cent of pores may be responsible for 50 per cent of the total flow in media with high pore-size variability. The equivalent conductivity remains within Hashin and Shtrickman bounds.

Spatial correlation reduces the probability of small pores being next to large ones. There is more focused channelling of fluid flow along interconnected regions of high conductivity and the hydraulic conductivity is higher than in an uncorrelated medium with the same pore size distribution.

The equivalent hydraulic conductivity in anisotropic correlated media increases as the correlation length parallel to the flow direction increases relative to the transverse correlation. The hydraulic conductivity in anisotropic uncorrelated pore networks is bounded by the two extreme 'parallel-of-series' and 'series-of-parallel' tube configurations. Flow analysis shows a pronounced decrease in tortuosity when pore size and spatial correlation in the flow direction are higher than in the transverse direction.

While Poiseuille flow defines the governing role of pore size on hydraulic conductivity, the numerical results presented in this manuscript show the combined effects of pore size distribution and variance, spatial correlation and anisotropy (either in mean pore size or in correlation length). In particular, results show that the proper analysis of hydraulic conductivity requires adequate interpretation of preferential flow paths or localization along interconnected high conductivity paths, often prompted by variance and spatial correlation. The development of flow localization will impact a wide range of flow related conditions including the performance of seal layers and storativity, invasion and mixed fluid flow, contaminant migration and remediation, efficiency in resource recovery, the formation of dissolution pipes in reactive transport and the evolution of fine migration and clogging.

ACKNOWLEDGMENTS

Support for this research was provided by the National Science Foundation and by DOE/NETL Methane Hydrate Project under contract DE-FC26–06NT42963.

REFERENCES

Acharya, R.C., Van Der Zee, S.E.A.T.M. & Leijnse, A., 2004. Porosity-permeability properties generated with a new 2-parameter 3D hydraulic pore-network model for consolidated and unconsolidated porous media, *Adv. Water Resour.,* **27,** 707–723.

Albrecht, K.A., Logsdon, S.D., Parker, J.C. & Baker, J.C., 1985. Spatial variability of hydraulic properties in the emporia series, *Soil Sci. Soc. Am. J.,* **49,** 1498–1502.

Al-Kharusi, A.S. & Blunt, M.J., 2007. Network extraction from sandstone and carbonate pore space images, *J. Pet. Sci. Eng.,* **56,** 219–231.

Al-Kharusi, A.S. & Blunt, M.J., 2008. Multiphase flow predictions from carbonate pore space images using extracted network models, *Water Resour. Res.,* **44,** W06S01, doi:10.1029/2006WR005695.

Al-Raoush, R.I. & Wilson, C.S., 2005. Extraction of physically realistic pore network properties from three-dimensional synchrotron X-ray microtomography images of unconsolidated porous media system, *J. Hydrol.,* **300,** 44–64.

Balhoff, M.T., Thompson, K.E. & Hjortsø, M., 2007. Coupling pore-scale networks to continuum-scale models of porous media, *Comput. Geosci.,* **33,** 393–410.

Benson, C., 1993. Probability distributions for hydraulic conductivity of compacted soil liners, *J. Geotech. Eng.,* **119**(3), 471–486.

Benson, C. & Daniel, D., 1994. Minimum thickness of compacted soil liners: II. Analysis and case histories, *J. Geotech. Eng.,* **120**(1), 153–172.

Bernabé, Y. & Bruderer, C., 1998. Effect of the variance of pore size distribution on the transport properties of heterogeneous networks, *J. geophys. Res.,* **103**(B1), 513–525.

Bjerg, P.L., Hinsby, K., Christensen, T.H. & Gravesen, P., 1992. Spatial variability of hydraulic conductivity of an unconfined sandy aquifer determined by a mini slug test, *J. Hydrol.,* **135,** 107–122.

Blunt, M.J., 2001. Flow in porous media—pore-network models and multiphase flow, *Curr. Opin. Colloid Interface Sci.,* **6,** 197–207.

Bruderer, C. & Bernabé, Y., 2001. Network modeling of dispersion: transition from Taylor dispersion in homogeneous networks to mechanical dispersion in very heterogeneous ones, *Water Resour. Res.,* **37**(4), 897–908.

Bruderer-Weng, C., Cowie, P., Bernabé, Y. & Main, I., 2004. Relating flow channelling to tracer dispersion in heterogeneous networks, *Adv. Water Resour.,* **27,** 843–855.

Bryant, S.L., Mellor, D.W. & Cade, C.A., 1993. Physically representative network models of transport in porous media, *Am. Inst. Chem. Eng. J.,* **39**(3), 387–396.

Cassel, D.K., 1983. Spatial and temporal variability of soil physical properties following tillage of Norfolk loamy sand, *Soil Sci. Soc. Am. J.,* **47,** 196–201.

Dagan, G., 1979. Models of groundwater flow in statistically homogeneous porous formations, *Water Resour. Res.,* **15**(1), 47–63.

David, C., 1993. Geometry of flow paths for fluid transport in rocks, *J. geophys. Res.,* **98,** 267–278.

Degroot, D.J., 1996. Analyzing spatial variability of in situ soil properties: uncertainty in the geologic environment, from theory to practice, in *Proceedings of the Uncertainty '96,* Geotechnical special publication No. 58, Madison, Wisconsin, pp. 210–238.

Ditmars, J.D., Baecher, G.B., Edgar, D.E. & Dowding, C.H., 1988. Radioactive waste isolation in salt: a method for evaluating the effectiveness of site characterization measurements, Final report ANL/EES-TM-342, Argonne National Laboratory.

Dong, H. & Blunt, M., 2009. Pore-network extraction from micro-computerized-tomography images, *Phys. Rev. E,* **80,** 036307, doi:10.1103/PhysRevE.80.036307.

Duffera, M., White, J.G. & Weisz, R., 2007. Spatial variability of southeastern U.S. coastal plain soil physical properties: implications for site-specific management, *Geoderma,* **137,** 327–339.

Fatt, I. 1956a. The network model of porous media, I. Capillary pressure characteristics, *Trans. Am. Inst. Min. Metall. Pet. Eng.,* **207,** 144–159.

Fatt, I. 1956b. The network model of porous media, II. Dynamic properties of a single size tube network, *Trans. Am. Inst. Min. Metall. Pet. Eng.,* **207,** 160–163.

Fatt, I. 1956c. The network model of porous media, III. Dynamic properties of networks with tube radius distribution, *Trans. Am. Inst. Min. Metall. Pet. Eng.,* **207,** 164–177.

Fredd, C.N. & Fogler, H.S., 1998. Influence of transport and reaction on wormhole formation in porous media, *Am. Inst. Chem. Eng. J.,* **44**(9), 1933–1949.

Freeze, R.A., 1975. A stochastic-conceptual analysis of one-dimensional groundwater flow in nonuniform homogeneous media, *Water Resour. Res.,* **11**(5), 725–741.

Griffiths, D.V. & Fenton, G.A., 1993. Seepage beneath water retaining structures founded on spatially random soil, *Géotechnique,* **43**(4), 577–587.

Griffiths, D.V. & Fenton, G.A., 1997. Three-dimensional seepage through spatially random soil, *J. Geotech. Geoenviron. Eng.,* **123**(2), 153–160.

Griffiths, D.V., Paice, G.M. & Fenton, G.A., 1994. Finite element modeling of seepage beneath a sheet pile wall in spatially random soil, in *Computer Methods and Advances in Geomechanics*, pp. 1205–1209, eds, Siriwardane, H.J. & Zaman, M.M., Balkema, Rotterdam.

Gutjahr, A., Gelhar, L.W., Bakr, A.A. & MacMillan, J.R., 1978. Stochastic analysis of spatial variability in subsurface flows 2. Evaluation and application, *Water Resour. Res.,* **14**(5), 953–959.

Hashin, Z. & Shtrikman, S., 1962. A variational approach to the theory of the effective magnetic permeability of multiphase materials, *J. appl. Phys.,* **33**(10), 3125–3131.

Hoefner, M.L. & Fogler, H.S., 1988. Pore evolution and channel formation during flow and reaction in porous media, *Am. Inst. Chem. Eng. J.,* **34**(1), 45–54.

Hoeksema, R.J. & Kitanidis, P.K., 1985. Analysis of the spatial structure of properties of selected aquifers, *Water Resour. Res.,* **21**(4), 563–572.

Hoshen, J. & Kopelman, R., 1976. Percolation and cluster distribution. 1. Cluster multiple labeling technique and critical concentration algorithm, *Phys. Rev. B,* **14**(8), 3438–3445.

Kang, Q., Tsimpanogiannis, I.N., Zhang, D. & Lichtner, P.C., 2005. Numerical modeling of pore-scale phenomena during CO_2 sequestration in oceanic sediments, *Fuel Process. Tech.,* **86,** 1647–1665.

Kampel, G, Goldsztein, G.H. & Santamarina, J.C. 2008. Plugging of porous media and filters: maximum clogged porosity, *Appl. Phys. Lett.,* **92,** 084101, doi:10.1063/1.2883947.

Lacasse, S. & Nadim, F., 1996. Uncertainties in characterizing soil properties, in *Proceedings of the Uncertainty '96,* Geotechnical special publication No. 58, Madison, Wisconsin, pp. 49–75.

Landau, L.D. & Lifshitz, E.M., 1960. *Electrodynamics of Continuous Media,* Pergamon Press, Oxford.

Laudone, G.M., Matthews, G.P. & Gane, P.A.C., 2008. Modelling diffusion from simulated porous structures, *Chem. Eng. Sci.,* **63,** 1987–1996.

Libardi, P.L., Reichardt, K., Nielsen, D.R. & Biggar, J.W., 1980. Simple field methods for estimating soil hydraulic conductivity, *Soil Sci. Soc. Am. J.,* **44**(1), 3–7.

Lindquist, W.B., Venkatarangan, A., Dunsmuir, J. & Wong, T., 2000. Pore and throat size distributions measured from synchrotron X-ray tomographic images of Fontainebleau sandstones, *J. geophys. Res.,* **105**(B9), 21 509–21 527.

Matheron, G., 1967. *Eléments Pour une Théorie des Milieux Poreux,* Masson, Paris.

Mu, D., Liu, Z-S., Huang, C. & Djilali, N., 2008. Determination of the effective diffusion coefficient in porous media including Knudsen effects, *Microfluid Nanofluid,* **4**(3), 257–260.

Narsilio, G.A., Buzzi, O., Fityus, S., Yun, T.S. & Smith, D.W., 2009. Upscaling of Navier-Stokes equations in porous media: theoretical, numerical and experimental approach, *Comput. Geotech.,* **36**(7), 1200–1206.

Prat, M., 2002. Recent advances in pore-scale models for drying of porous media, *Chem. Eng. J.,* **86,** 153–164.

Reeves, P.C. & Celia, M.A., 1996. A functional relationship between capillary pressure, saturation, and interfacial area as revealed by a pore-scale network model, *Water Resour. Res.,* **32**(8), 2345–2358.

Sahimi, M., 1994. *Applications of Percolation Theory,* p. 258, Taylor & Francis, London.

Stauffer, D. & Aharony, A., 1992. *Introduction to Percolation Theory,* 2nd edn, p. 181, Taylor & Francis, London.

Suicmez, V.S., Piri, M. & Blunt, M.J., 2008. Effects of wettability and pore-level displacement on hydrocarbon trapping, *Adv. Water Resour.,* **31,** 503–512.

Surasani, V.K., Metzger, T. & Tsotas, E., 2008. Consideration of heat transfer in pore network modelling of convective drying, *Int. J. Heat Mass Transfer,* **51,** 2506–2518.

Taskinen, A., Sirvio, H & Bruen, M., 2008. Generation of two-dimensionally variable saturated hydraulic conductivity fields: model theory, verification and computer program, *Comput. Geosci.,* **34,** 876–890.

Tsimpanogiannis, I.N. & Lichtner, P.C., 2003. Pore network study of methane clathrate hydrate dissociation, *EOS, Trans. Am. geophys. Un.,* **84**(46) (Abstract OS51B-0848).

Tsimpanogiannis, I.N. & Lichtner, P.C., 2006. Pore-network study of methane hydrate dissociation, *Phys. Rev. E,* **74,** 056303, doi:10.1103/PhysRevE.74.065303.

Valvatne, P.H., 2004. Predictive Pore-scale modeling of multiphase flow, *PhD thesis*, Imperial College, London.

Warren, J.E. & Price, H.S., 1961. Flow in heterogeneous porous media, *Soc. Pet. Eng.,* **1,** 153–169.

Warrick, A.W. & Nielsen, D.R., 1980. Spatial variability of soil physical properties in the field, in *Applications of Soil Physics,* pp. 319–344, ed. Hill, D., Academic Press, Inc., New York, NY.

Wiener, O., 1912. Abhandlungen der mathematisch, *Physischen Klasse der Königlichen Sächsischen Gesellschaft der Wissenschaften,* **32,** 509.